Electronic Supplementary Material (ESI) for Inorganic Chemistry Frontiers.

Supporting Information

Dendritic NiS_2@Co-N-C nanoarchitectures as bifunctional electrocatalysts for long-life Zn-air batteries

Yanli Ruan,[ab] *Hang Xu,*[a] *Haikuo Lei,*[c] *Wenjuan Xue,*[b] *Tianyu Wang,*[a] *Shidong Song,*[a] *Yangyang Yu,*[a] *Gui-Rong Zhang*[a] *and Donghai Mei*[*bc]

[a] School of Chemical Engineering and Technology, Tiangong University, Tianjin, P. R. China.

[b] School of Environmental Science and Engineering, Tiangong University, Tianjin, P.R. China.

[c] School of Materials Science and Engineering, Tiangong University, Tianjin, P.R. China.

* Corresponding authors. E-mail addresses: ruanyanli@tiangong.edu.cn (Y.Ruan), dhmei@tiangong.edu.cn (D. Mei).

S1. Material characterization

The samples were analyzed by X-ray diffractometry (XRD) on Rigaku D/ MAX-2500. X-ray photoelectron spectroscopy (XPS) data were collected by Thermofisher K-Alpha, The C 1s peak was used to calibrate the binding energy at 284.5 eV. Nitrogen adsorption-desorption measurement is performed on a MicroMertics analyzer (ASAP 2020 PLUS HD88), and the specific surface area (SSA) is measured using Brunauer-Emmett-Teller (BET). Morphological information was obtained by Gemini SEM500 field emission scanning electron microscopy (FESEM) and transmission electron microscopy (TEM: JEOL jem-2100). Energy Dispersive X-ray Spectroscopy (EDS) was performed on EDAX OCTANE SUPER to observe the element distributions in SEM images.

S2. Preparation and testing for oxygen reaction catalyst

All electrochemical measurements were made at room temperature (~25 ℃) using a 760E bipotentiostat (Shanghai Chenhua Instrument, China) in a conventional three-electrode cell. The suspension was prepared by ultrasonic dispersion of 5 mg catalyst in 50 μL Nafion (5 wt %) solution and 500 μL ethanol-water (volume ratio 5:4.5) solution. Working electrode adopts polished glassy carbon electrode (diameter: 3 mm). A certain volume of catalyst ink is uniformly dispersed on the surface of a rotating disk electrode (RDE) or a rotating ring disk electrode (RRDE), and then dried in air to obtain an electrode coated with a catalyst film. Commercial Pt/C (20 wt %) and IrO_2 were used as control catalysts. The catalyst loading is 0.5 mg cm^{-2}.

The ORR measurements were made in an O_2-saturated 0.1 M KOH solution using a saturated calomel electrode (SCE) as a reference electrode and a graphite carbon rod s a counter electrode. All measured potentials were converted to an RHE scale by a calibration equation, $E_{RHE}=E_{SCE}+0.059pH+0.241$. Thin-film rotating disk electrode (RDE) technique was employed to evaluate the ORR activities of different electrocatalysts. Linear sweep voltammetry (LSV) curves were

recorded in an O_2-saturated 0.1 M KOH solution with RDE rotation rates of 400, 625, 900, 1225, 1600, 2025, and 2500 rpm at a scanning rate of 10 mV s^{-1}, and the catalyst was tested in the potential range of 0.2-1.1 V (vs. RHE). The accelerated durability test of the catalyst was performed by recording the LSV curves before and after 2000 cycles in 50 mV s^{-1} O_2 saturated 0.1 M KOH solution. The long-term stability test of the catalyst was characterized by chronoamperometry for 18000 s. A methanol durability test was performed by adding 3 M methanol at 1200 s by chronoamperometry to characterize its methanol resistance. The electron transfer number (n) of ORR is calculated by Kouteck-Levich (K-L) equation [1,2]:

$$\frac{1}{j} = \frac{1}{j_L} + \frac{1}{j_K} = \frac{1}{B\omega^{\frac{1}{2}}} + \frac{1}{j_K} \quad (1)$$

$$B = 0.62nFC_O D^{\frac{2}{3}} \nu^{-\frac{1}{6}} \quad (2)$$

where j is the measured current density, j_K is the dynamic current density, j_L is the limit current density, ω is the angular velocity of electrode rotation, n is the electron transfer number, F is the Faraday constant (96485 C mol^{-1}), C_o is the volume concentration of O_2 (1.2×10^{-6} mol cm^{-3} in 0.1 M KOH) and D is the diffusion coefficient of O_2 (1.9 × 10-5 cm^2 s^{-1} in 0.1 M KOH). ν is the kinetic viscosity of electrolyte (0.01 cm^2 s^{-1} for 0.1 M KOH).

In the RRDE test, hydrogen peroxide (H_2O_2%) yield and electron transfer number (n) were calculated using the following formula [3,4]:

$$HO_2^-\% = \frac{200i_r}{N(i_d + \frac{i_r}{N})} \quad (3)$$

$$n = \frac{4i_d}{i_d + \frac{i_r}{N}} \quad (4)$$

where i_d and i_r are disk current and ring current, respectively. N is the current collection efficiency of Pt ring (0.42).

The OER measurements were conducted in an O_2-saturated 1 M KOH solution using Hg/HgO and a graphite as reference and counter electrodes, respectively. All measured potentials were converted to RHE scales by a calibration equation, $E_{RHE}=E_{Hg/HgO}+0.059pH+0.098$**.** The OER polarization curve was measured at a potential range of 0.2−1.0 V (vs. RHE) at a scanning rate of 5 mV s^{-1}. The Tafel slope was calculated from the LSV curve by plotting the relationship between the overpotential (η) and the logarithm of current density (j). The electrochemically active surface area (ECSA) of the samples was estimated based on the electrochemical double-layer capacitance (C_{dl}) and determined by CV curves recorded at different scanning rates in the non-Faraday interval (0.95-1.05 V).

$$C_{dl} = \frac{j_a - j_c}{2v} = \frac{\Delta j}{2v} \quad (5)$$

Where Δj is the difference between the anode and cathode current density recorded under the selected potential range, and v is the scan rate. The electrochemical impedance spectroscopy (EIS) test was performed at 1.60 V (vs. RHE), the frequency range is 0.1 Hz-10 kHz, and the amplitude is 10 mV.

The oxygen electrode activity (ΔE) is evaluated by the potential of the OER at a current density of 10 mA cm^{-2} and the half-wave potential of ORR:

$$\Delta E = E_{OER} - E_{ORR} = E_{j=10} - E_{\frac{1}{2}} \quad (6)$$

S3. Zinc-air battery assembly and testing

NiS_2@Co-N-C/CNF catalyst and Nafion adhesive (5%) were weighed with a mass ratio of 7:3, and ultrasonic dispersion was carried out in DMF solution to obtain uniform catalyst slurry. Then the catalyst slurry was uniformly coated on the nickel foam to prepare the air cathode (mass load: 1 mg

cm^{-2}). A gas diffusion layer (GDL) is pressed on the back of the nickel foam to make oxygen enter the battery smoothly. For comparison, the same method was used to prepare Pt/C, a Pt/C and IrO_2 mixed catalyst with a mass ratio of 1:1 to prepare an air cathode. A 0.2 mm polished zinc foil was used for the anode, and a mixture of 0.2 M $Zn(OAc)_2$ and 6 M KOH was used as the liquid electrolyte of the rechargeable ZABs, and a self-made liquid ZABs was assembled. All tests were carried out in an ambient atmosphere with a constant current discharge-charge cycle in the LAND test system using CHI760E electrochemical workstation with open circuit potential as the initial potential. The polarization curves were recorded at a scanning rate of 5 mV s^{-1} and the current and power were normalized to the geometric surface area of the air cathode.

To assemble flexible solid state ZABs, a 0.08 mm polished zinc foil was used as the anode, and the catalyst-coated nickel foam was used as the air cathode. 1 g PVA in 10 mL deionized water under 95 °C for 2 h to form a uniform viscous solution, then slowly add a certain amount of a mixed solution of 18 M KOH and 0.2 M $Zn(OAc)_2$ dropwise with constant heating and stirring for 20 min to form electrolyte.

Under the current density of 1 mA cm^{-2}, the performance of constant current discharge-charge cycle was tested, discharging for 5 min and charging for 5 min. the formula for calculating the power density of a ZABs is as follows:

$$P = IV \tag{7}$$

Where I is the discharge current density, and V is the voltage. The calculation formula of specific capacity is as follows [5]:

$$Specific\ capacity = \frac{current * service\ hours}{weigh\ of\ consumed\ zinc} \tag{8}$$

S4. Computational methodology

All periodic density functional theory (DFT) calculations were carried out using the CP2K code employed a mixed Gaussian and planewave basis sets [6,7]. The generalized gradient approximation functional of Perdew, Burke, and Enzerhof (PBE) [8] was used to described the exchange-correlation potential. Core electrons were represented with norm-conserving Goedecker-Teter-Hutter pseudopotentials[9-11]. The valence electron wavefunction was expanded in a double-zeta basis set with polarization functions[12] along with an auxiliary plane wave basis set with an energy cutoff of 400 Ry. The force convergence criteria of 0.001 hartree/bohr was used. Each adsorption structure was optimized with the Broyden-Fletcher-Goldfarb-Shanno (BGFS) algorithm with SCF convergence criteria of 1.0×10^{-8} au. The van der Waals dispersion interaction was compensated using the DFT-D3 scheme[13] with an empirical damped potential term in all calculations.

Three model surfaces, i.e., NiS_2, Co-N-C, and NiS_2/Co-N-C were constructed. The periodic single NiS_2 layer structure was modeled as a c(2×2) supercell slab containing 12 Ni atoms and 24 O atoms (see **Figure S13**). A vacuum height of 12 Å in the *z* direction was inserted between the NiS_2 surface slabs to eliminate any unphysical interaction. Similarly, a periodic Co-N-C coordinated surface structure ($C_{42}N_4Co_1$) was constructed (see **Figure S14**). The vacuum space in the *z* direction was set to 14.8 Å, ensuring there is no interactions within the periodic boundary. The simulation box size is 9.8400 × 12.7825 × 14.8000 $Å^3$. The NiS_2@Co-N-C surface structure was constructed by placing a NiS_2 layer over the Co-N-C substrate (see **Figure S15**). The simulation box parameters for the NiS_2@Cu-N-C catalyst is 10.5488 × 12.1807 × 17.9846 $Å^3$. After optimization, it is found that the averaged distance between two layered structures is 3.45 Å.

The typical four-electron ORR/OER reaction mechanism was considered in this work. Under acidic conditions, the overall reaction can be represented as:

$$O_2 + 4(H^+ + e^-) \rightarrow 2H_2O \qquad \Delta G_0 = 4.92\ eV \tag{9}$$

The Gibbs free energy difference (ΔG_0) is 4.92 eV for the ORR reaction at p = 1 bar and T = 298.15 K. The reverse reaction process of ORR is the OER reaction. The reaction was generally believed to proceed in four steps [14-16]:

$$O_2 + (H^+ + e^-) + * \rightarrow OOH* \tag{10}$$

$$OOH* + (H^+ + e^-) + * \rightarrow H_2O + O* \tag{11}$$

$$O* + (H^+ + e^-) + * \rightarrow OH* \tag{12}$$

$$OH* + (H^+ + e^-) + * \rightarrow H_2O \tag{13}$$

where * represents the active site of the catalyst, and OOH*, O*, and OH* represent the species adsorbed on the active site. At the standard condition (p = 1 bar and T = 298.15), the Gibbs free energy of $H^+ + e^-$ equals the Gibbs free energy of 1/2H_2. The Gibbs free reaction energy (ΔG), which is calculated by the binding strengths between the catalyst and the ORR intermediates:

$$\Delta G = \Delta E + \Delta E_{ZPE} - T\Delta S \tag{14}$$

where ΔE is the DFT calculated adsorption energy of the intermediate. Herein, ΔE of OOH*, O* and OH* intermediates are all referred to gaseous H_2O and H_2:

$$\Delta E_{OOH*} = E_{OOH*} - E_* - (2E_{H_2O} - \frac{3}{2}E_{H_2}) \tag{15}$$

$$\Delta E_{O*} = E_{O*} - E_* - (E_{H_2O} - E_{H_2}) \tag{16}$$

$$\Delta E_{OH*} = E_{OH*} - E_* - (E_{H_2O} - \frac{1}{2}E_{H_2}) \tag{17}$$

where E_{H_2O} and E_{H_2} are the calculated DFT energies of H_2O and H_2 molecules in the gas phase using the approaches outlined by Nørskov *et al.* [9,11]

The zero-point energy (ZPE) contribution is given by:

$$E_{ZPE} = \sum_i \frac{hv_i}{2} \tag{18}$$

where h and v_i are the Plank's constant and vibrational frequencies which are calculated based on the localized harmonic oscillator approximation with a displacement of 0.01 Å. Only the mobile ascorbates and the atoms at the active site were considered while all other atoms on the catalyst surface are treated as fixed. The vibrational entropy contributions (S) can be calculated below:

$$S = k_B \sum_i \left(\frac{hv_i}{k_B T \left(e^{hv_i / k_B T} - 1 \right)} - ln\left(1 - e^{-hv_i / k_B T} \right) \right) \tag{19}$$

Because the high-spin ground state of an oxygen molecule is difficult to accurately describe in DFT calculation, the Gibbs free energy of O_2(g) is derived as

$$G_{O_2} = 2G_{H_2O} - 2G_{H_2} + 4.92\ eV \tag{20}$$

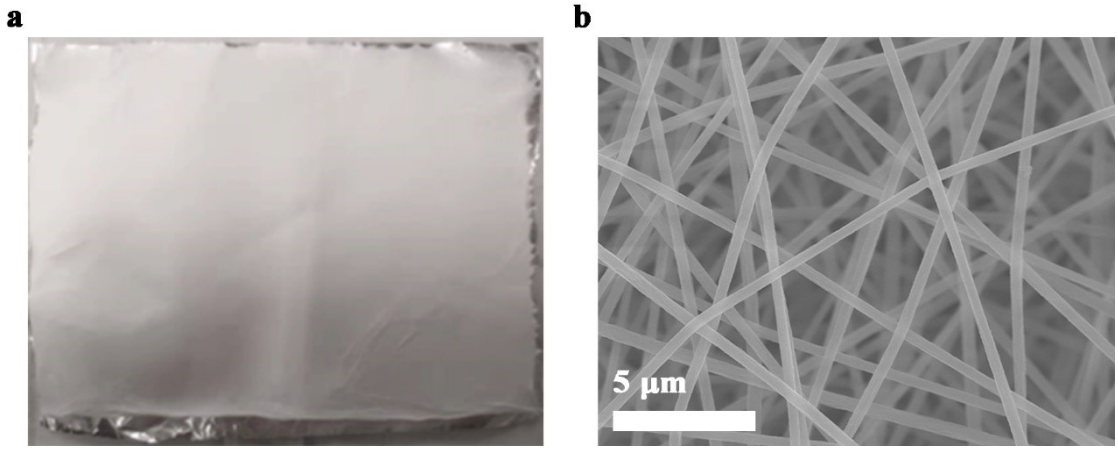

Fig. S1. (a) The optical photograph of PAN nanofiber film by electrospinning method, (b) FESEM image of PAN nanofiber film.

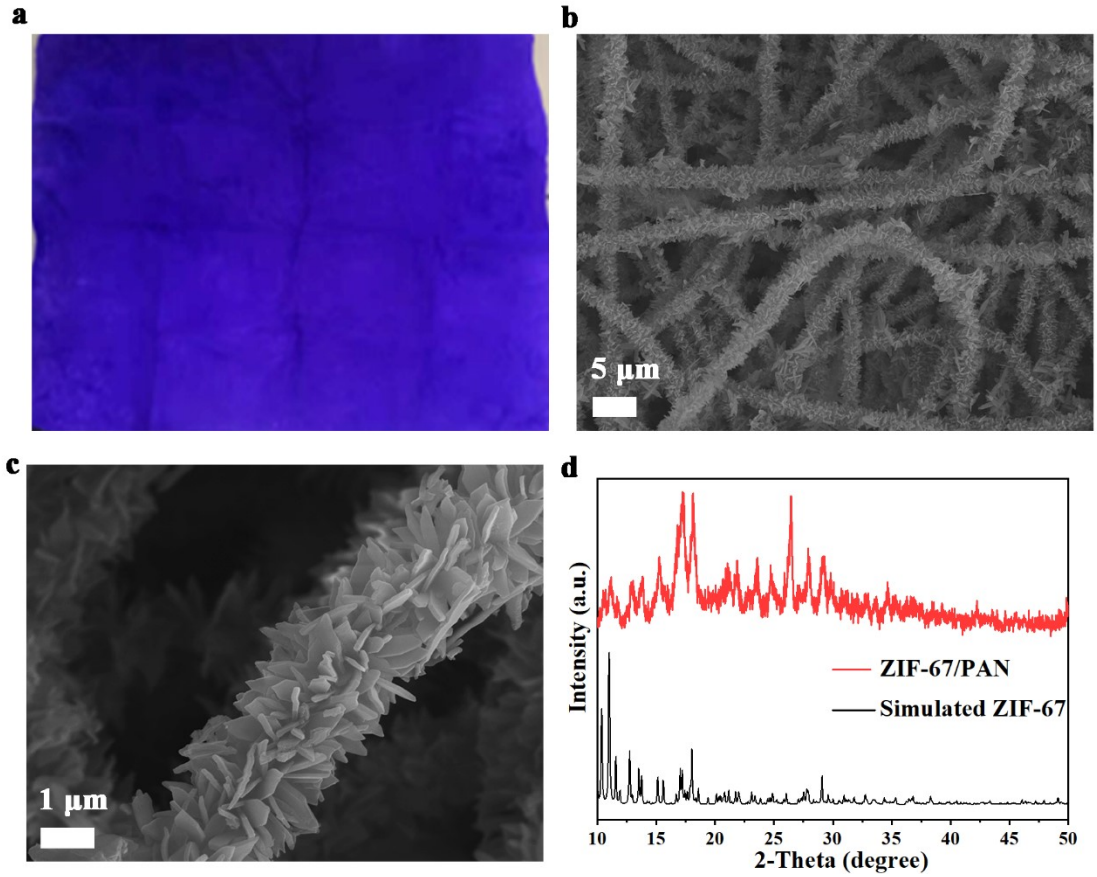

Fig. S2. (a) The optical photograph of the prepared ZIF-67/PAN, (b, c) FESEM images of the prepared ZIF-67/PAN, (d) XRD pattern of the prepared ZIF-67/PAN.

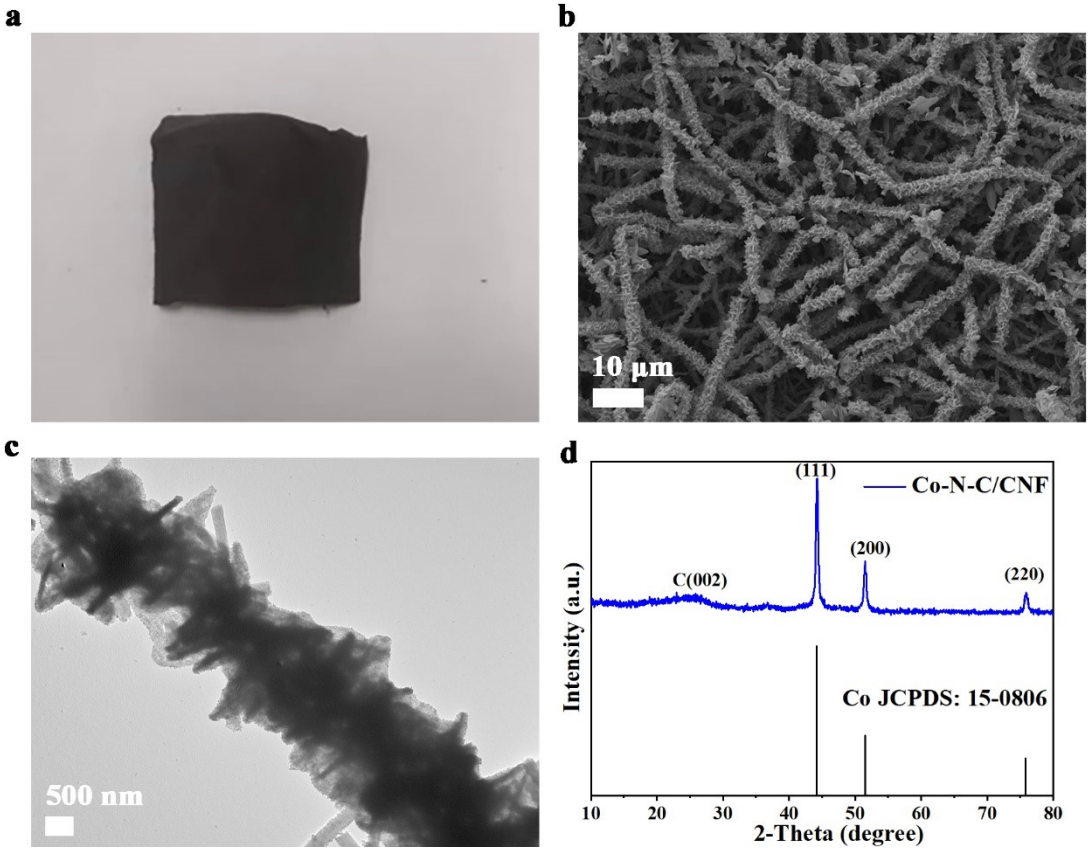

Fig. S3. (a) Optical photo of Co-N-C/CNF catalyst prepared by carbonization under N_2 atmosphere, (b) FESEM images of Co-N-C/CNF, (c) Corresponding TEM image, (d) XRD pattern of Co-N-C/CNF.

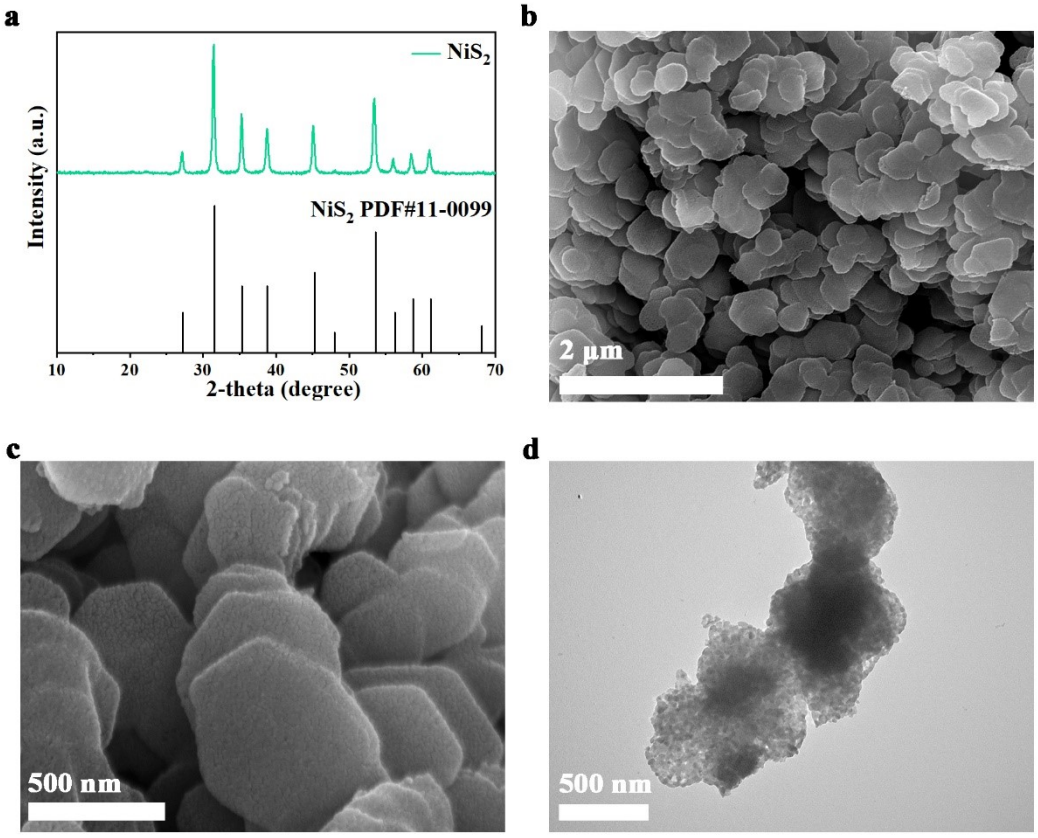

Fig. S4. (a) XRD pattern of NiS_2, (b,c) FESEM images of NiS_2, (d) Corresponding TEM image.

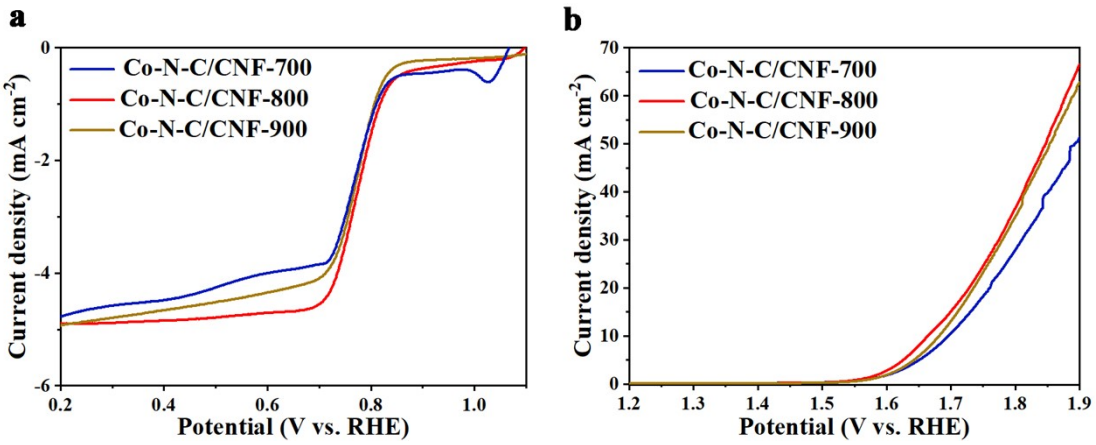

Fig. S5. (a) The ORR and (b) OER LSV curves of Co-N-C/CNF catalyst from 700 ℃,800 ℃ and 900 ℃.

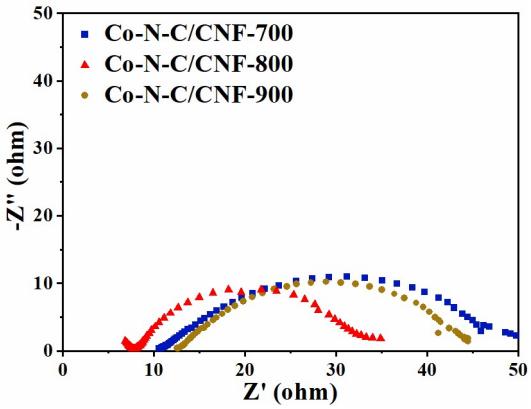

Fig. S6. EIS Nyquist plots of Co-N-C/CNF catalyst from 700 ℃,800 ℃and 900 ℃.

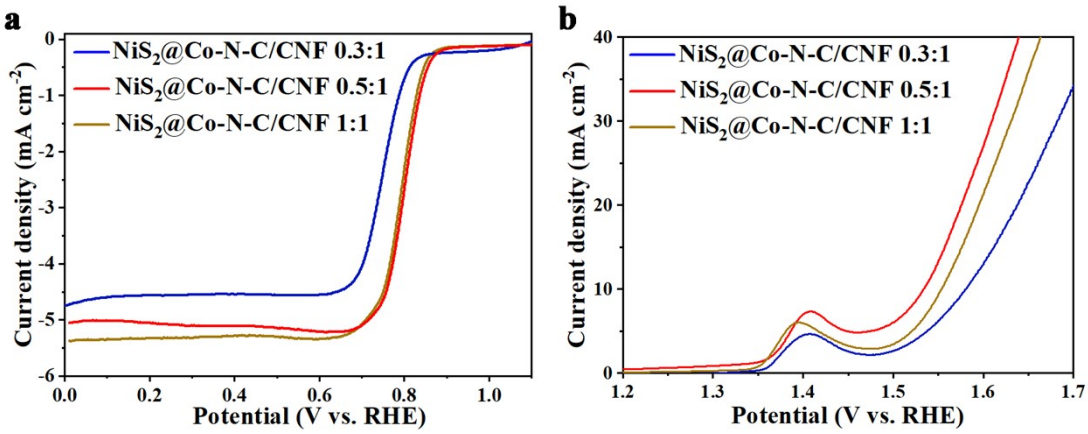

Fig. S7. (a) The ORR and (b) OER LSV curves of NiS_2@Co-N-C/CNF catalyst from the different mass ratios between NiS_2 and Co-N-C/CNF.

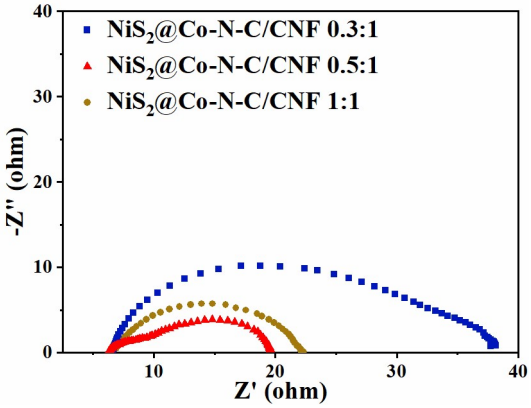

Fig. S8. EIS Nyquist plots of NiS_2@Co-N-C/CNF catalyst from the different mass ratio between NiS_2 and Co-N-C/CNF.

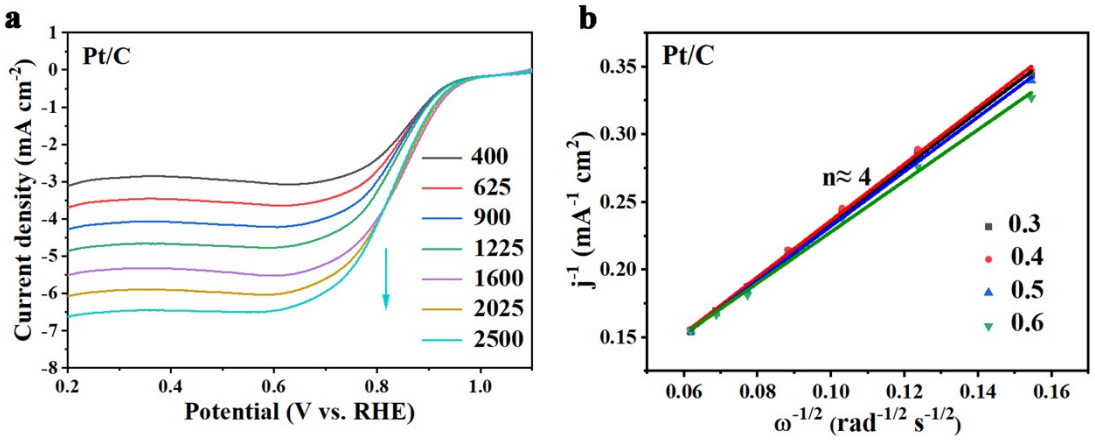

Fig. S9. (a) LSV curves of Pt/C at various rotation speeds, (b) K-L plots for different voltages according to the LSV curves in (a).

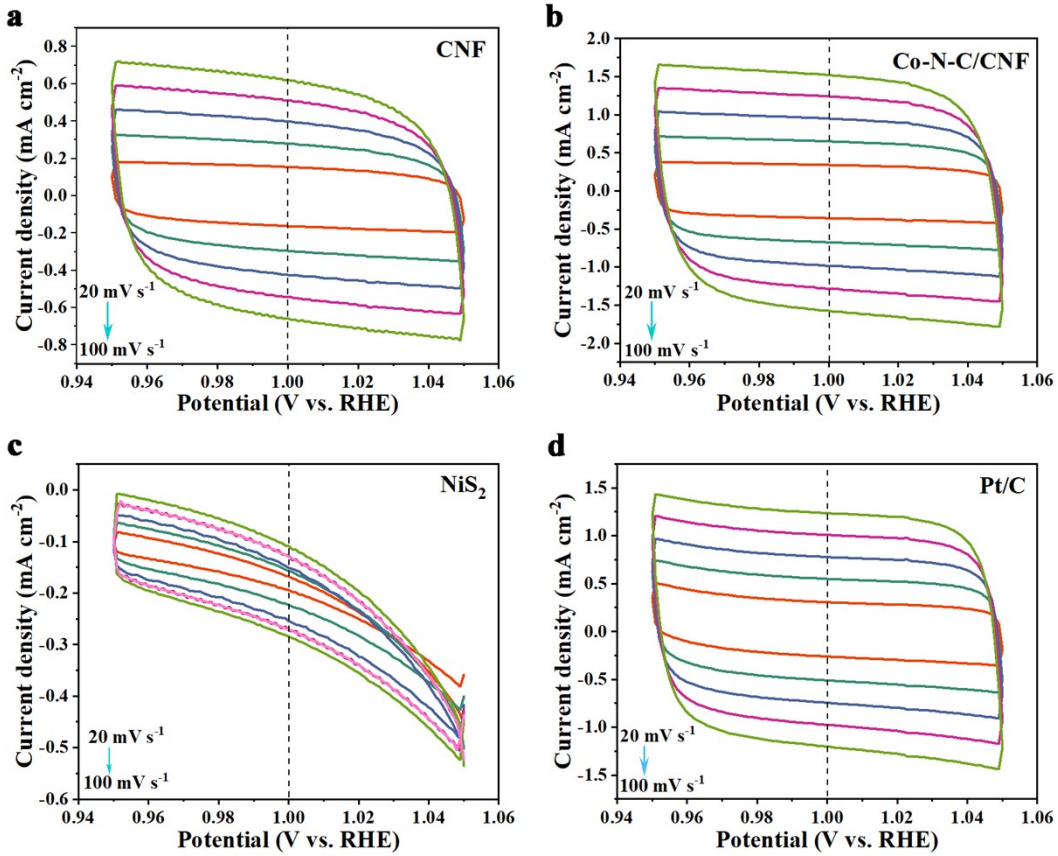

Fig. S10. The CV curves of the (a) CNF, (b) NiS_2, (c) Co-N-C/CNF, and (d) Pt/C samples

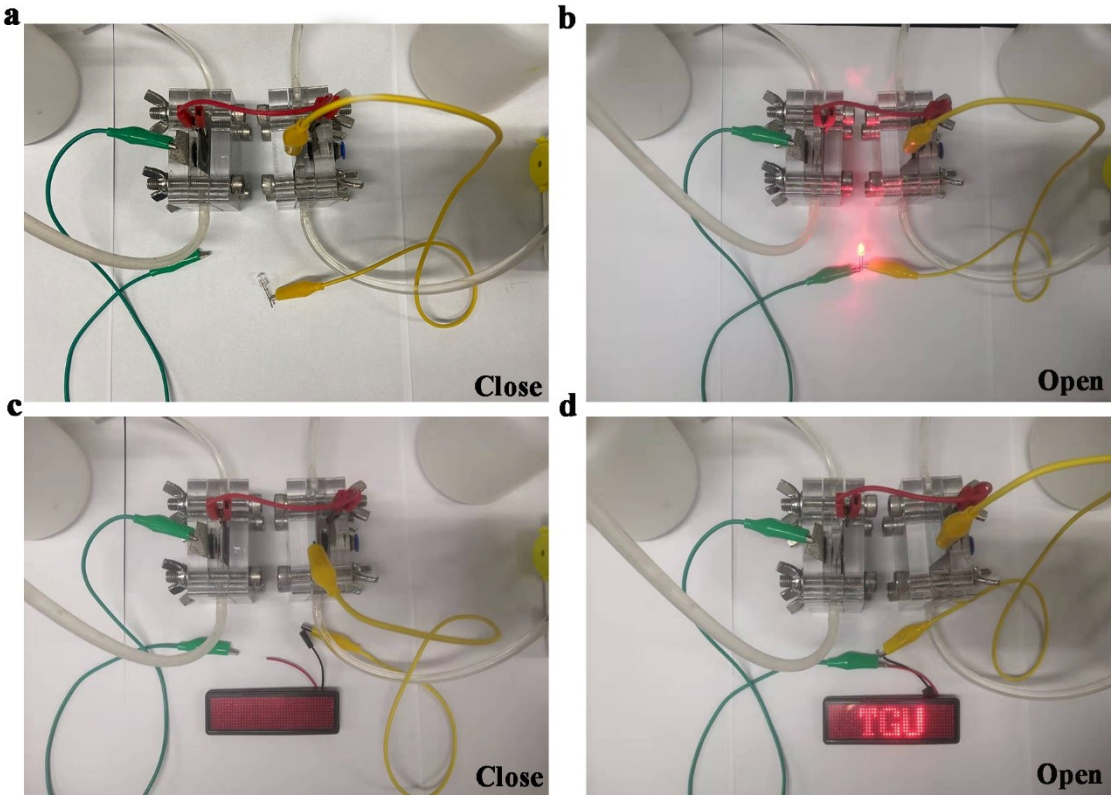

Fig. S11. Optical photos of (a,b) a small bulb and (c,d) LED powered by the assembled liquid ZABs (Two) in series.

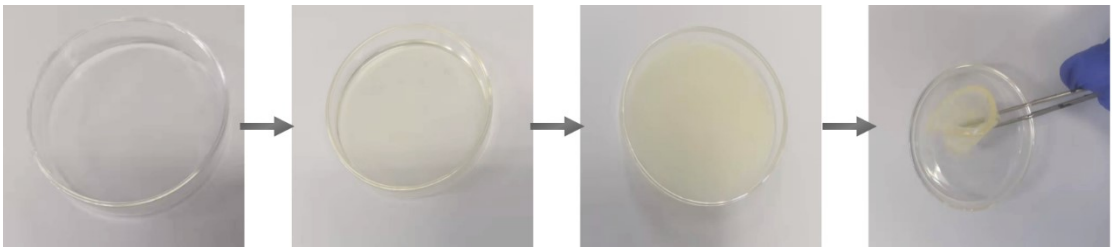

Fig. S12. Optical photo of PVA-KOH gel electrolyte.

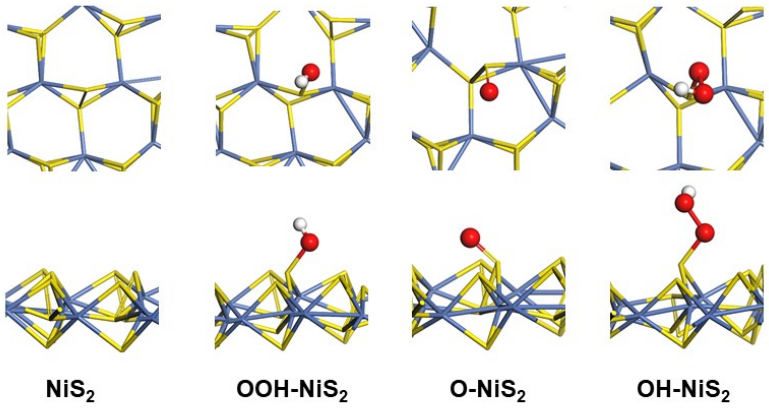

Fig. S13. Optimized structures (top and side views) of ORR/OER intermediates adsorbed on the NiS_2.

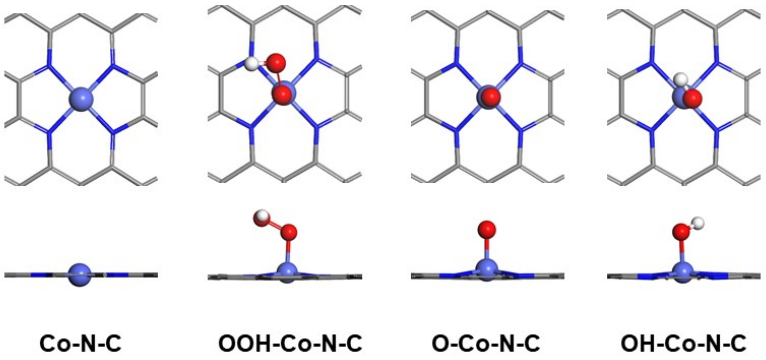

Fig. S14. Optimized structures (top and side views) of ORR/OER intermediates adsorbed on the Co-N-C.

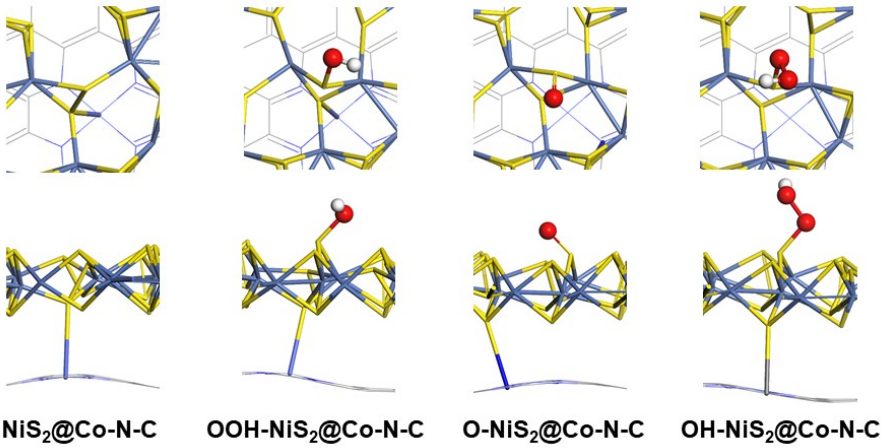

Fig. S15. Optimized structures (top and side views) of ORR/OER intermediates adsorbed on the NiS_2@Co-N-C.

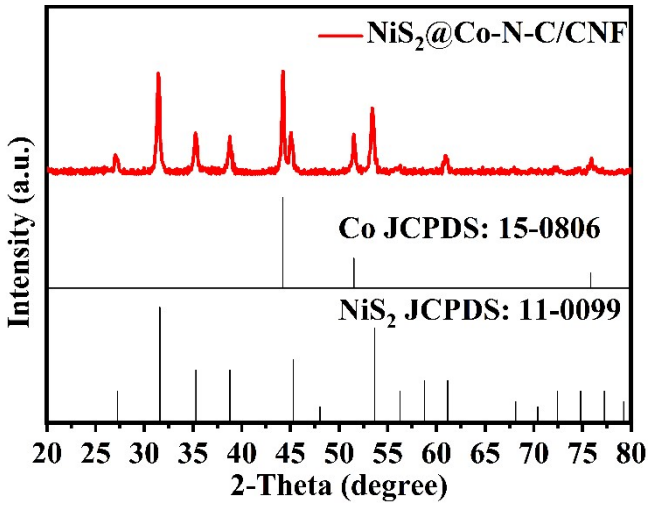

Fig. S16. XRD pattern of NiS_2@Co-N-C/CNF after 100 cycles.

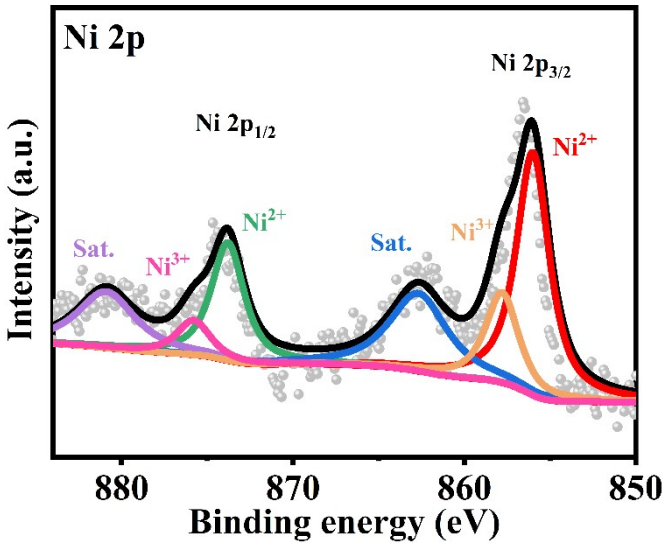

Fig. S17. High resolution Ni 2p of NiS_2@Co-N-C/CNF after 100 cycles.

Table S1. The Comparison of ORR catalytic performance of this work with other non-noble metal-based catalysts recently reported (0.1M KOH).

Catalysts	E_{onset} (V)	$E_{1/2}$ (V)	Tafel slopes (mV dec^{-1})	Reference
N-CoS_2 YSSs	0.95	0.81	52	[17]
W_2N/WC	0.93	0.81	58.13	[18]
CoSA/N,S-HCS	0.96	0.85	-	[19]
FeCo/Co_2P@NPCF	0.85	0.79	62	[20]
Co_3O_{4-X}/NG	0.96	0.84	-	[21]
Co_2P/NPG-900	0.94	0.81	64.1	[22]
NiFe@N-CFs	0.94	0.82	58	[23]
MnO/Co@NGC	0.91	0.82	-	[24]
$NiCo_2S_4$/$RGO_{0.02}$	0.90	0.78	-	[25]
Co-Ni-S@NSPC	0.95	0.82	-	[26]
Co_9S_8/C	0.89	0.78	-	[27]
NiS_2/CoS_2	0.90	0.79	-	[28]
CoFe/N-HCSs	0.901	0.791	59	[2]
CoFeP@C	0.90	0.80	66.6	[29]
NiS_2@Co-N-C/CNF	**0.90**	**0.80**	**56**	**[This work]]**

Table S2. The Comparison of OER catalytic performance of this work with other non-noble metal-based catalysts recently reported (1M KOH).

Catalysts	Overpotential@ 10 mA cm^{-2} (mV)	Tafel slopes (mV dec^{-1})	Reference
N-CoS_2 YSS	278	56	[17]
CoSA/N,S-HCS	306	38.1	[19]
Co_3O_4-X/NG	296	84.85	[21]
Co_2P/NPG-900	320	66.6	[22]
NiS_2/CoS_2	295	51	[28]
CoFe/N-HCSs	292	58	[2]
CoFeP@C	336	82.5	[29]
FeCo-NCNTs	320	61.5	[30]
N-Mo-holey G	300	47	[31]
CoNC-NB2	350	98	[32]
Co/N@CNTs@CNMF-800	310	61.3	[33]
AlFeCoNiCr	240	52	[34]
(Fe,Co)SPPc-900-sp	353	53	[35]

CoFe-N-CNTs/CNFs-900	320	92	[36]
Co_3O_4/Mn_3O_4/CNX@CNFs	400	105	[37]
Fe_2/Co_1-GNCL	350	70	[38]
Fe@N-CNT/HMCS	340	76	[39]
Co@N-C/PCNF	289	91.86	[40]
Co/CoFe@NC	300	49	[1]
NiS_2@Co-N-C/CNF	**300**	**57**	**This work**

Table S3. The Comparison of liquid Zn-air batteries performance of this work with other non-noble metal-based catalysts recently reported.

Catalysts	Open circuit voltage (OCV)	Power density (mW cm^{-2})	Cycling current density (mA cm^{-2})	Stability (h)	Reference
N-CoS_2YSS	1.41	81	10	165	[17]
CoSA/N,S-HCS	1.50	173.1	10	333	[19]
Co_3O_4-X/NG	1.49	166	5	63	[21]
CoFe/N-HCSs	1.387	96.5	5	160	[2]
CoNC-NB2	1.50	246	2	140	[32]
Co/N@CNTs@CNMF-800	1.52	133	10	190	[33]
(Fe,Co)SPPc-900-sp	1.47	158.6	2	50	[35]
CoFe-N-CNTs/CNFs-900	1.462	-	10	85	[36]
FeNi/N-LCN	1.49	162	5	1100	[41]
Co-UA-OCB	1.475	142	10	100	[42]
NiFe/N-CNT	1.48	300	5	100	[43]
CoFe/Co@NCNT/NG	1.4	161	2	100	[44]
FeP/Fe_2O_3@NPCA	1.42	130	5	160	[45]
Fe-Co_4N@N-C	1.46	105	5	36.7	[46]
Co NPs/N,S-CNTs	1.433	153.8	5	120	[47]
NiS_2@Co-N-C/CNF	**1.47**	**181**	**5**	**1050**	**This work**
NiS_2@Co-N-C/CNF	**1.47**	**181**	**10**	**600**	**This work**

Supplementary Reference

[1] Y. Niu, X. Teng, S. Gong, M. Xu, S. Sun and Z. Chen, Engineering two-phase bifunctional oxygen electrocatalysts with tunable and synergetic components for flexible Zn-air batteries, *Nano-Micro Lett.*, 2021, **13**, 126.

[2] J. Li, Y. Kang, W. Wei, X. Li, Z. Lei and P. Liu, Well-dispersed ultrafine CoFe nanoalloy decorated N-doped hollow carbon microspheres for rechargeable/flexible Zn-air batteries, *Chem. Eng. J.*, 2021, **407**, 127961.

[3] C. C. Yang, S. F. Zai, Y. T. Zhou, L. Du and Q. Jiang, Fe_3C-Co nanoparticles encapsulated in a hierarchical structure of N-doped carbon as a multifunctional electrocatalyst for ORR, OER, and HER, *Adv. Funct. Mater.*, 2019, **29**, 1901949.

[4] X. Peng, L. Zhang, Z. Chen, L. Zhong, D. Zhao, X. Chi, X. Zhao, L. Li, X. Lu, K. Leng, C. Liu, W. Liu, W. Tang and K. P. Loh, Hierarchically porous carbon plates derived from wood as bifunctional ORR/OER electrodes, *Adv. Mater.*, 2019, **31**, 1900341.

[5] Y. Zhao, Q. Lai, J. Zhu, J. Zhong, Z. Tang, Y. Luo and Y. Liang, Controllable construction of core-shell polymer@zeolitic imidazolate frameworks fiber derived heteroatom-doped carbon nanofiber network for efficient oxygen electrocatalysis, *Small*, 2018, **14**, 1704207.

[6] J. Vandevondele, M. Krack, F. Mohamed and M. Parrinello, Quickstep : Fast and accurate density functional calculations using a mixed Gaussian and plane waves approach, *Comput. Phys. Commun.*, 2005, **167**, 103-128.

[7] T. D. Kühne, M. Iannuzzi, M. Del Ben, V. V Rybkin, P. Seewald, V. Weber, F. Stein, T. Laino, R. Z. Khaliullin, O. Schütt, F. Schiffmann, J. Wilhelm, S. Chulkov, M. H. Bani-hashemian, U. Borštnik, M. Taillefumier, A. S. Jakobovits, R. Schade, I. Bethune, M. Krack, A. Lazzaro, H. Pabst, A. Glöß, M. Lass, J. Vandevondele, M. Guidon, S. Andermatt, N. Holmberg, G. K. Schenter, C. Plessl, M. Watkins, A. Hehn, A. Bussy, F. Belleflamme, G. Tabacchi, C. J. Mundy, M. Iannuzzi, M. Del Ben, V. V Rybkin, P. Seewald, F. Stein, T. Laino, J. Wilhelm, S. Chulkov and M. H. Bani-hashemian, CP2K : An electronic structure and molecular dynamics software package - Quickstep : efficient and accurate elect, *J. Chem. Phys.*, 2020, **152**, 194103.

[8] J. P. Perdew, K. Burke and M. Ernzerhof, Generalized gradient approximation made simple, *Phy. Rev. Lett.*, 1996, **77**, 3865-3868.

[9] S. Goedecker, M. Teter and J. Hutter, Separable dual-space Gaussian pseudopotentials, *Phy. Rev. B*, 1996, **54**, 1703-1710.

[10] C. Hartwigsen, S. Goedecker and J. Hutter, Relativistic separable dual-space Gaussian pseudopotentials from H to Rn, *Phy. Rev. B*, 1998, **58**, 3641-3662.

[11] M. Krack, M. Parrinello and M. Planck, All-electron ab-initio molecular dynamics, *Phys. Chem. Chem. Phys.*, 2000, **2**, 2105-2112.

[12] J. Vandevondele and J. Hutter, Gaussian basis sets for accurate calculations on molecular systems in gas and condensed phases, *J. Chem. Phys.*, 2007, **127**, 114105.

[13] S. Grimme, J. Antony, S. Ehrlich and H. Krieg, A consistent and accurate ab initio parametrization of density functional dispersion correction (DFT-D) for the 94 elements H-Pu, *J. Chem. Phys*., 2010, **132**, 154104.

[14] J. K. Nørskov, J. Rossmeisl, A. Logadottir, L. Lindqvist, D. Lyngby and H. Jo, Origin of the overpotential for oxygen reduction at a fuel-cell cathode, *J. Phys. Chem. B*, 2004, **108**, 17886-17892.

[15] J. Rossmeisl, Z. W. Qu, H. Zhu, G. J. Kroes and J. K. Nørskov, Electrolysis of water on oxide surfaces, *J. Electroanal. Chem.*, 2007, **607**, 83-89.

[16] I. C. Man, H. Su, F. Calle-vallejo, H. A. Hansen, J. I. Martínez, N. G. Inoglu, J. Kitchin, T. F. Jaramillo, J. K. Nørskov and J. Rossmeisl, Universality in oxygen evolution electrocatalysis on oxide surfaces, *ChemCatChem*, 2011, **3**, 1159-1165.

[17] X. F. Lu, S. L. Zhang, E. Shangguan, P. Zhang, S. Gao and X. W. Lou, Nitrogen-doped cobalt pyrite yolk-shell hollow spheres for long-life rechargeable Zn-air batteries, *Adv. Sci.*, 2020, **7**, 2001178.

[18] J. Diao, Y. Qiu, S. Liu, W. Wang, K. Chen, H. Li, W. Yuan, Y. Qu and X. Guo, Interfacial engineering of W_2N/WC heterostructures derived from solid-state synthesis: A highly efficient trifunctional electrocatalyst for ORR, OER, and HER, *Adv. Mater.*, 2020, **32**, 1905679.

[19] Z. Zhang, X. Zhao, S. Xi, L. Zhang, Z. Chen, Z. Zeng, M. Huang, H. Yang, B. Liu, S. J. Pennycook and P. Chen, Atomically dispersed cobalt trifunctional electrocatalysts with tailored coordination environment for flexible rechargeable Zn-air battery and self-driven water splitting, *Adv. Energy Mater.*, 2020, **10**, 2002896.

[20] Q. Shi, Q. Liu, Y. Ma, Z. Fang, Z. Liang, G. Shao, B. Tang, W. Yang, L. Qin and X. Fang, High-

performance trifunctional electrocatalysts based on FeCo/Co_2P hybrid nanoparticles for zinc-air battery and self-powered overall water splitting, *Adv. Energy Mater*., 2020, **10**, 1903854.

[21] J. Qin, Z. Liu, D. Wu and J. Yang, Optimizing the electronic structure of cobalt via synergized oxygen vacancy and Co-N-C to boost reversible oxygen electrocatalysis for rechargeable Zn-air batteries, *Appl. Catal. B*, 2020, **278**, 119300.

[22] Q. Shao, Y. Li, X. Cui, T. Li, H. Wang, Y. Li, Q. Duan and Z. Si, Metallophthalocyanine-based polymer-derived Co_2P nanoparticles anchoring on doped graphene as high-efficient trifunctional electrocatalyst for Zn-air batteries and water splitting, *ACS Sustain. Chem. Eng.*, 2020, **8** 6422-6432.

[23] Y. Niu, X. Teng, S. Gong and Z. Chen, A bimetallic alloy anchored on biomass-derived porous N-doped carbon fibers as a self-supporting bifunctional oxygen electrocatalyst for flexible Zn–air batteries, *J. Mater. Chem. A*, 2020, **8**, 13725-13734.

[24] T. Meng, B. Mao and M. Cao, In situ coupling of MnO and Co@N-doped graphite carbon derived from prussian blue analogous achieves high-performance reversible oxygen electrocatalysis for Zn-air batteries, *Inorg. Chem.*, 2021, **60**, 10340-10349.

[25] Y. Liang, Q. Gong, X. Sun, N. Xu, P. Gong and J. Qiao, Rational fabrication of thin-layered $NiCo_2S_4$ loaded graphene as bifunctional non-oxide catalyst for rechargeable zinc-air batteries, *Electrochim. Acta*, 2020, **342**, 136108.

[26] W. Fang, H. Hu, T. Jiang, G. Li and M. Wu, N- and S-doped porous carbon decorated with in-situ synthesized Co-Ni bimetallic sulfides particles: A cathode catalyst of rechargeable Zn-air batteries, *Carbon*, 2019, **146**, 476-485.

[27] L. Li, L. Song, H. Guo, W. Xia, C. Jiang, B. Gao, C. Wu, T. Wang and J. He, N-doped porous carbon nanosheets decorated with graphitized carbon layer encapsulated Co_9S_8 nanoparticles: An efficient bifunctional electrocatalyst for the OER and ORR, *Nanoscale,* 2019, **11**, 901-907.

[28] Y. Cao, X. Zheng, H. Zhang, J. Zhang, X. Han, C. Zhong, W. Hu and Y. Deng, Interface engineering of NiS_2/CoS_2 nanohybrids as bifunctional electrocatalysts for rechargeable solid state Zn-air battery, *J. Power Sources*, 2019, **437**, 226893.

[29] L. Gao, S. Chang and Z. Zhang, High-quality CoFeP nanocrystal/N, P dual-doped carbon composite as a novel bifunctional electrocatalyst for rechargeable Zn-air battery, *ACS Appl. Mater. Interfaces*, 2021, **13**, 22282-22291.

[30] S. Lin, L. Xi, L. Zhang, J. Feng, Y. Zhao and A. Wang, Highly active Fe centered FeM-N-doped carbon (M = Co/Ni/Mn): A general strategy for efficient oxygen conversion in Zn-air battery, *Chem. Eng. J.*, 2021, **424**, 130559.

[31] P. Du, K. Hu, J. Lyu, H. Li, X. Lin, G. Xie, X. Liu, Y. Ito and H. Qiu, Anchoring Mo single atoms/clusters and N on edge-rich nanoporous holey graphene as bifunctional air electrode in Zn-air batteries, *Appl. Catal. B*, 2020, **276**, 119172.

[32] H. Luo, W. Jiang, S. Niu, X. Zhang, Y. Zhang, L. Yuan, C. He and J. Hu, Self-catalyzed growth of Co-N-C nanobrushes for efficient rechargeable Zn-air batteries, *Small*, 2020, **16**, 2001171.

[33] T. Liu, J. Mou, Z. Wu, C. Lv, J. Huang and M. Liu, A facile and scalable strategy for fabrication of superior bifunctional freestanding air electrodes for flexible zinc-air batteries, *Adv. Funct.l Mater.*, 2020, **30**, 2003407.

[34] G. Fang, J. Gao, J. Lv, H. Jia, H. Li, W. Liu, G. Xie, Z. Chen, Y. Huang, Q. Yuan, X. Liu, X. Lin, S. Sun and H. Qiu, Multi-component nanoporous alloy/(oxy)hydroxide for bifunctional oxygen electrocatalysis and rechargeable Zn-air batteries, *Appl. Catal. B*, 2020, **268**, 118431.

[35] L. Chen, L. Cui, Z. Wang, X. He, W. Zhang and T. Asefa, Co_8FeS_8/N,S-doped carbons derived from Fe-Co/S-bridged polyphthalocyanine: Efficient dual-function air-electrode catalysts for rechargeable Zn-air batteries, *ACS Sustain. Chem. Eng.*, 2020, **8**, 13147-13158.

[36] S. Wang, J. Wang, X. Wang, L. Li, J. Qin and M. Cao, Carbon hybrid with 3D nano-forest architecture in-situ catalytically constructed by CoFe alloy as advanced multifunctional electrocatalysts for Zn-air batteries-driven water splitting, *J. Energy Chem.*, 2021, **53**, 422-432.

[37] L. Li, L. Fu, R. Wang, J. Sun, X. Li, C. Fu, L. Fang and W. Zhang, Cobalt, manganese zeolitic-imidazolate-framework-derived Co_3O_4/Mn_3O_4/CNx embedded in carbon nanofibers as an efficient bifunctional electrocatalyst for flexible Zn-air batteries, *Electrochim. Acta*, 2020, **344**, 136145.

[38] Y. Wei, L. Sun, M. Wang, J. Hong, L. Zou, H. Liu, Y. Wang, M. Zhang, Z. Liu, Y. Li, S. Horike, K. Suenaga and Q. Xu, Fabricating dual-atom iron catalysts for efficient oxygen evolution reaction: A heteroatom modulator approach, *Angew. Chem. Int. Ed.*, 2020, **59**, 16013-16022.

[39] J. Liu, H. Xu, H. Li, Y. Song, J. Wu, Y. Gong, L. Xu, S. Yuan, H. Li and P. M.Ajayane, In-situ formation of hierarchical 1D-3D hybridized carbon nanostructure supported nonnoble transition metals for efficient electrocatalysis of oxygen reaction, *Appl. Catal. B*, 2019, **243**, 151-160.

[40] Q. Lu, H. Wu, X. Zheng, Y. Chen, A. L. Rogach, X. Han, Y. Deng and W. Hu, Encapsulating cobalt nanoparticles in interconnected N-doped hollow carbon nanofibers with enriched Co-N-C moiety for enhanced oxygen electrocatalysis in Zn-air batteries, *Adv. Sci.*, 2021, **8**, 2101438.

[41] X. Li, Y. Liu, H. Chen, M. Yang, D. Yang, H. Li and Z. Lin, Rechargeable Zn-air batteries with outstanding cycling stability enabled by ultrafine FeNi nanoparticles-encapsulated N-doped carbon nanosheets as a bifunctional electrocatalyst, *Nano Lett.*, 2021, **21**, 3098-3105.

[42] T. Fu, G. Li, Y. Xiang, Y. Tang, D. Cai, S. Jiang, Y. Xue, Z. Xiong, Y. Si and C. Guo, Hierarchical cobalt-nitrogen-doped carbon composite as efficiently bifunctional oxygen electrocatalyst for rechargeable Zn-air batteries, *J. Alloys Compd.*, 2021, **878**, 160349.

[43] H. Lei, Z. Wang, F. Yang, X. Huang, J. Liu, Y. Liang, J. Xie, M. S. Javed, X. Lu, S. Tan and W. Mai, NiFe nanoparticles embedded N-doped carbon nanotubes as high-efficient electrocatalysts for wearable solid-state Zn-air batteries, *Nano Energy*, 2020, **68**, 104293.

[44] P. Zhu, J. Gao and S. Liu, Facile in situ coupling CoFe/Co nanoparticles and N-doped carbon nanotubes/graphitic nanosheets as bifunctional oxygen electrocatalysts for rechargeable Zn-air batteries, *J. Power Sources*, 2020, **449**, 227512.

[45] K. Wu, L. Zhang, Y. Yuan, L. Zhong, Z. Chen, X. Chi, H. Lu, Z. Chen, R.Zou, T. Li, C. Jiang, Y. Chen, X. Peng and J. Lu, An Iron-Decorated Carbon Aerogel for Rechargeable Flow and Flexible Zn–Air Batteries, *Adv. Mater.*, 2020, **32**, 2002292.

[46] Q. Xu, H. Jiang, Y. Li, D. Liang, Y. Hu, C. Li, In-situ enriching active sites on co-doped Fe-Co4N@N-C nanosheet array as air cathode for flexible rechargeable Zn-air batteries, *Appl. Catal. B*, 2019, **256**, 117893.

[47] Q. Yan, R. Sun, L. Wang, J. Feng, L. Zhang and A. Wang, Cobalt nanoparticles/ nitrogen, sulfur-codoped ultrathin carbon nanotubes derived from metal organic frameworks as high-efficiency electrocatalyst for robust rechargeable zinc-air battery, *J. Colloid Interface Sci.*, 2021, **603**, 559-571.